

## Far-field modelling of THM processes in rock salt formations

Florian Zill<sup>1</sup>, Christian B. Silbermann<sup>2</sup>, Tobias Meisel<sup>1</sup>, Fabiano Magri<sup>3,4</sup> & Thomas Nagel<sup>5,6,7</sup>

**Published**

29th November 2024

<https://doi.org/10.5802/ogeo.20>

**Edited by**

Eleni Gerolymatou  
Technische Universität Clausthal  
Clausthal, Germany

**Reviewed by**

Ayman Abed  
Chalmers University of Technology  
Gothenburg, Sweden

Reviewer B  
anonymous

Reviewer C  
anonymous

**Correspondence**

Florian Zill  
Helmholtz Centre for Environmental  
Research – UFZ, Leipzig, Germany  
Permoserstr. 15  
04318 Leipzig, Germany  
Technische Universität Bergakademie  
Freiberg, Freiberg, Germany  
[florian.zill@ufz.de](mailto:florian.zill@ufz.de)



This article is licensed under the Creative Commons Attribution NonCommercial ShareAlike 4.0 License.



Open Geomechanics is member of the  
Centre Mersenne for Open Scientific Publishing

<sup>1</sup> Helmholtz Centre for Environmental Research – UFZ, Leipzig, Germany

<sup>2</sup> Technische Universität Bergakademie Freiberg, Freiberg, Germany

<sup>3</sup> Federal Office for the Safety of Nuclear Waste Management, Germany

<sup>4</sup> Freie Universität Berlin, Germany

<sup>5</sup> Freiberg Center for Water Research – ZeWaF, Freiberg, Germany.

**Abstract.** Glaciation cycles are one aspect to be considered in assessing the safety of deep geological repository sites for long-term radioactive waste storage. This study examines the impact of time-dependent boundary conditions and thermo-hydro-mechanical (THM) couplings on geological formations under glaciation-induced stresses, pressures and temperature changes. Using OpenGeoSys, an open-source finite element simulator, we analyzed various process couplings to understand the underlying physical processes and numerical instabilities. We simulated vertical cross-sections of geological models relevant to nuclear waste repository sites, incorporating comprehensive geological data to capture the formations' heterogeneity and structural features. A viscoelastic material model was used for rock salt strata to account for dislocation creep and pressure-solution creep. The study benefited from rigorous automation of the entire simulation workflow, making the setup suitable for evaluating actual repository sites regarding integrity criteria. Although the modeled rock salt strata were hydraulically deactivated, results were highly dependent on hydraulic boundary conditions. Groundwater flow significantly altered the geological temperature profile via advective heat transport and influenced the temperature-dependent creep behavior. The rock salt creep law, applied over the extensive timescales at hand, approached the limits of the Finite Element Method (FEM) with small-strain assumptions. Throughout the modeled glacial cycle, the salt strata exhibit low deviatoric stresses. Fluid pressure and dilatancy criteria are not violated in the repository during the modeled period.

**Keywords.** rock salt, creep, glaciation, nuclear waste repository, OpenGeoSys

# 1. Introduction

The goal stated per the German Site Selection Act (StandAG) [Bundesministerium für Umwelt, Naturschutz, nukleare Sicherheit und Verbraucherschutz, 2023] is to safely store the German nuclear waste for 1 million years. This time frame may cover multiple glacial cycles, which have been shown to significantly shape the deformation history of salt strata by geological observations [White, 1992], modeling studies [Lang and Hampel, 2023, Lang et al., 2014] and physical modeling [Hardt et al., 2023]. Thus, the effect of glacial cycles on potential deep geological repositories (DGR) in rock salt has to be investigated. This may include a significant impact on the mechanical and hydraulic properties, which could compromise the barrier integrity. Glacial cycles, consisting of cold periods (glacial phases) and warm periods (interglacial phases), have characterised the Pleistocene Ice Age. Interglacials are defined by abrupt increases in temperature, followed by a longer cold period [Emiliani, 1955]. Glacial cycles impose significant transient changes in thermal, hydraulic and mechanical conditions alike, e.g. with permafrost influencing the hydraulic flow field which in turn influences heat transport, additional mechanical stresses from the glacial load, as well as erosion and sedimentation [Fischer et al., 2021].

Rock salt is one of three potential host rock candidates considered in the German site selection process. A key characteristic of rock salt is its viscoplastic deformation behaviour. Viscoplasticity refers to the rate-dependent (viscous characteristic) and non-linear stress-strain behaviour with equilibrium hysteresis (elastoplastic characteristic). In the current study, we focus on the creep characteristics of rock salt using a viscoelastic model characterized by two main mechanisms: dislocation creep and pressure-solution creep [Bérest et al., 2019, Van Keken et al., 1993]. Dislocation creep describes the movement of dislocations through the crystal lattice and is highly sensitive to deviatoric stresses. It dominates the mechanical behavior of crystalline materials at low temperatures. Pressure-solution creep is a process enabled by the presence of a fluid phase, typically at grain

boundaries or present in inclusions, which facilitates the dissolution, transport and deposition of the material under pressure [Gratier et al., 2013]. It is hypothesized to dominate the mechanical behavior of rock salt at low deviatoric stresses [Bérest et al., 2019, Van Oosterhout et al., 2022]. This process accompanies grain rearrangement via intergranular sliding and grain rotation [Urai et al., 2008]. Figure 1 illustrates the microstructure and creep mechanisms of rock salt. Another feature of rock salt is its self-healing ability [Chen et al., 2013], which makes it well-suited for repairing excavation or construction-induced damage of underground caverns or repositories.

In terms of fluid transport, the interest in salt rocks is founded on their consideration as tight rocks due to their extremely low permeability [Peach, 1991, Schulze et al., 2001], rendering them interesting not only for hosting nuclear or chemo-toxic waste repositories but also for storage of oil, natural gas and hydrogen [Hunsche and Hampel, 1999, Małachowska et al., 2022]. In practise, rock salt is often considered impermeable [Gloyna and Reynolds, 1961] due to the lack of initial connectivity of pore space. Measurements often result in permeabilities below detection limit or they are associated with sample damage in the lab due to unloading. However, connectivity of pore space can be significantly affected by the presence or formation (during deformation) of micro-fissures and increase the permeability by multiple orders of magnitude [Stormont and Daemen, 1992].

It has been experimentally established that certain mechanical, hydraulic or thermal effects can cause the appearance of secondary porosity and permeability by, e.g., dilatant deformation or pore pressure exceeding tensile strength measures. Such states could thus potentially compromise barrier integrity, i.e. hydraulic tightness. Therefore, integrity criteria have been established that allow engineers to assess the extent to which prevailing loads and stress states comply with barrier integrity requirements [Düsterloh and Lux, 2004, Jobmann et al., 2017].

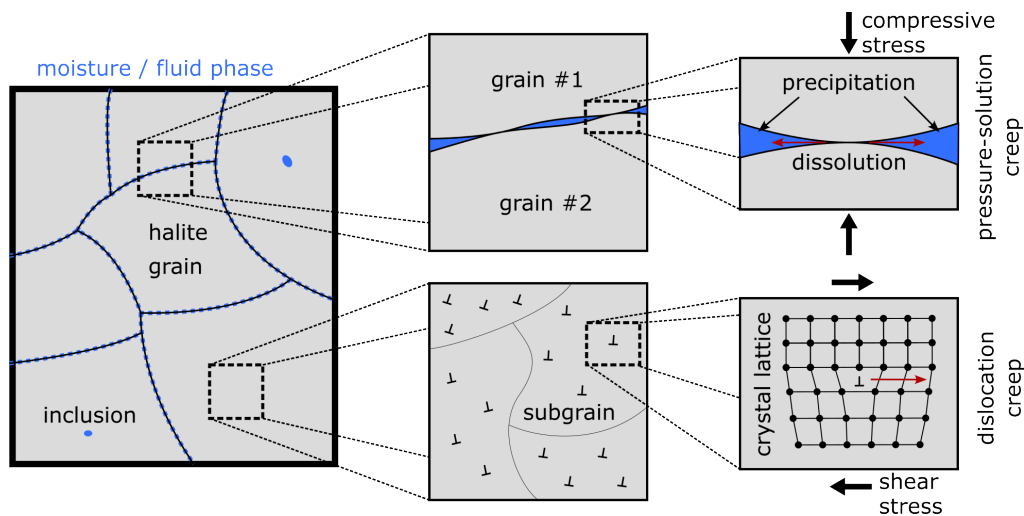


**Figure 1.** Microstructure and creep mechanisms in rock salt (after Wang and Zhang [2023])

Numerical modeling plays an important role in the comprehensive assessment and prediction of complex subsurface phenomena in geological formations. The Finite Element Method (FEM) is a well-established method for simulating models of real-world problems with coupled multi-field processes such as thermodynamics (T), hydraulics (H) and mechanics (M). This is especially useful for geological applications strongly influenced by all three processes. Further, an accurate geometry based on real-world geological data is essential for substantiated predictions. Finally, the representation of transient boundary conditions or source terms (e.g. the decay heat released by nuclear waste) and non-linearities due to state dependencies of material parameters can significantly influence simulation results and have to be modelled accordingly. Performance or convergence reasons might necessitate the need for simplifications. The complexity of such simulations resides mainly in the following aspects: the geological model, the physical processes, multi-step simulation sequences where one simulation departs from the results of the previous one, and the numerical behaviour of the coupled FEM model. Ensuring consistency of the results both from a physical and a numerical point of view is therefore often difficult to realize manually.

To facilitate this task, this study describes a semi-automated simulation workflow for complex far-field simulations that runs multi-step simulations and analyzes their results. We show this framework's applicability to the case of glacial loads and their impact in the far-field of a repository in bedded salt. The simulation model at the core of this study is composed of:

- (1) a layered geological model with bedded salt as a host rock for a DGR,
- (2) a two-component steady-state creep model for rock salt,
- (3) transient boundary conditions for glacial cycles and nuclear waste heat as a source term and
- (4) different THM coupling schemes.

We demonstrate the feasibility of such a far-field FEM study and analyze the different process interactions in the simulation results to achieve a comprehensive understanding of how the physical processes at hand interact. In the subsequent sections of this paper, we delve into the specifics of our numerical modeling approach, present our simulation results, and discuss the implications of our findings.

## 2. Governing equations

In this study, the subsurface is modeled as a multi-phasic porous medium using the Theory of Porous Media (TPM) [e.g., Ehlers and Wagner, 2019]. Specifically, a THM model for a fully saturated porous medium is considered. Based on the balance laws for energy, mass, and momentum, along with suitable constitutive relations, the following system of partial differential equations (PDEs) emerges [Pitz et al., 2023, Wang et al., 2021]:

$$T: (\rho c_p)^{\text{eff}} \frac{d_S T}{dt} + (\rho_{\text{FR}} c_{pF}) \text{grad } T \cdot \tilde{\mathbf{w}}_{\text{FS}} - \lambda^{\text{eff}} \text{div} [\text{grad } T] = q_T \quad (1)$$

$$\text{with } \tilde{\mathbf{w}}_{\text{FS}} = -\frac{k}{\mu_{\text{FR}}} [\text{grad } p - \rho_{\text{FR}} \mathbf{g}] \quad (2)$$

$$H: \rho_{\text{FR}} [\phi \beta_{pF} + (\alpha_B - \phi) \beta_{pS}] \frac{d_S p}{dt} - \rho_{\text{FR}} [\phi_F \beta_{TF} + (\alpha_B - \phi) \beta_{TS}] \frac{d_S T}{dt} + \rho_{\text{FR}} \alpha_B \text{div} \frac{d_S \mathbf{u}}{dt} + \text{div} (\rho_{\text{FR}} \tilde{\mathbf{w}}_{\text{FS}}) = q_p \quad (3)$$

$$M: \text{div} [\boldsymbol{\sigma}' - \alpha_B p \mathbf{I}] + \rho^{\text{eff}} \mathbf{g} = \mathbf{0} \quad (4)$$

Here, the temperature  $T$ , the pore pressure  $p$  and the displacement  $\mathbf{u}$  constitute the process variables. Further there are Biot's effective stress tensor ( $\boldsymbol{\sigma}'$ ), the Darcy velocity ( $\tilde{\mathbf{w}}_{\text{FS}}$ ), the heat source term ( $q_T$ ), the fluid mass source term ( $q_p$ ), the gravity acceleration vector ( $\mathbf{g}$ ) and the second order identity tensor ( $\mathbf{I}$ ). The time derivative with respect to the solid phase is denoted by  $d_S(\cdot)/dt$ . The volumetric thermal expansivity  $\beta_{TS}$  is related to the linear thermal expansivity  $\alpha_{TS}$  via  $\beta_{TS} = 3\alpha_{TS}$  in case of isotropy. The remaining variables relate to the material properties, whose meanings and values can be found in tables 4 and 5. The energy balance (T) describes transient heat transport, capturing both conductive and advective effects. The mass balance (H) accounts for the effects of different compressibilities and thermal expansions of the pore fluid and solid skeleton. Temperature changes induce pore pressure changes, which lead to fluid flow and pore space volume changes. Darcy's law relates pore pressure gradients and gravitational forces to fluid flow. The momentum balance (M) represents the quasistatic equilibrium of forces due to gravity, pore pressure, thermal expansion, and solid deformation. Effective stresses are derived from the solid material model.

## 3. Methods

The pre-processing, simulation execution and post-processing in this study were bundled in a comprehensive simulation workflow that was fully automated using Python and a workflow manager that was also used for a similar study on clay rock. [Meisel et al., 2024]

### 3.1. Geological model

In the pre-processing stage, finite element meshes were generated based on geological data from the KOSINA project [Bollingerfehr et al., 2018]. The geological data included very thin and discontinuous layers, which can only be discretized with an excessive number of elements or elements of inferior quality. Thus, some adjacent layers with similar material properties were combined to alleviate this problem. The resulting meshes still closely represented the complex structural features and heterogeneity of the geological formations under investigation. For improved performance, easier analysis and clearer visualisation, 2D cross-sections of these models were used for the simulations. The model examined in this study consists of 13 different stratigraphic layers. A cross-sectional view of the stratigraphy including the discretization can be seen in Figure 2. The finite element mesh consists of 64 459 quadratic order triangular elements with a median size of 118.7 m<sup>2</sup>.

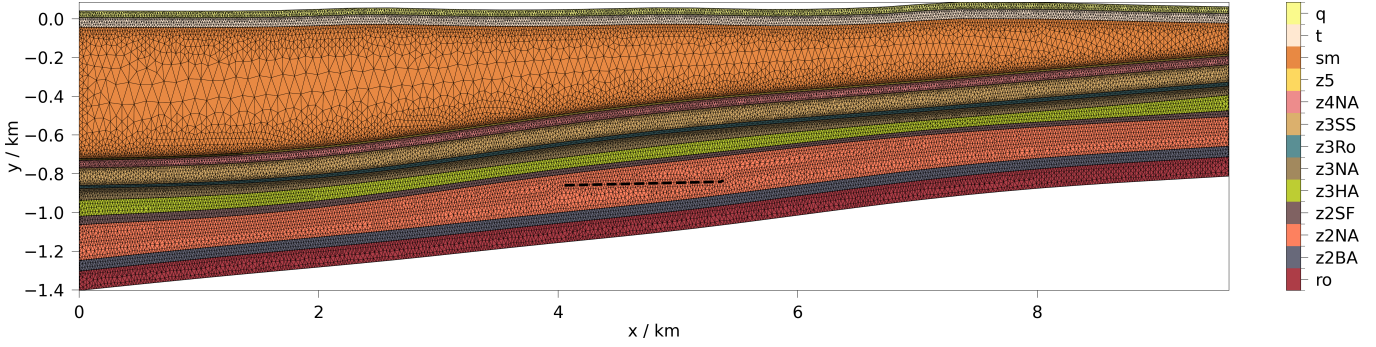


**Figure 2.** Unstructured mesh of model cross-section with stratigraphy (full names in the appendix) and repository outline (central thick dashed black line)

**Table 1.** Boundary conditions

| boundary | thermal                    | hydraulic  | mechanical  |
|----------|----------------------------|--|---|
| bottom   | $q_T = q_{\text{geo}}$     | closed   | $u_y = 0$   |
| left     | closed                     | $p = p_{\text{atm}} + p_{\text{hs}}$                                     | $u_x = 0$   |
| right    | closed                     | $p = p_{\text{atm}} + p_{\text{hs}} + p_{\text{glc}}(x_{\text{max}}, t)$ | $u_x = 0$   |
| top      | $T = T_{\text{top}}(x, t)$ | $p = p_{\text{atm}} + p_{\text{glc}}(x, t)$                              | $\sigma_{yy} = -p_{\text{atm}} - \rho_{\text{ice}} g h(t, x)$ |

### 3.2. Boundary conditions

The thermal, hydraulic and mechanical boundary conditions for our model are governed by periodic glacial cycles. While the onset of the next glacial cycle is highly uncertain and subject to future changes of climatic conditions [Haeberli et al., 2021], we base the model on historic data and assume a duration of 10,000 years for the warm periods, followed by cold periods of 80,000 years. Figure 3 shows the evolution of the surface temperature and the glacier size. The surface temperature evolves from 8.5 °C in warm periods to -1.5 °C in cold periods with transition periods of 10,000 years. The glacier grows from the right boundary of the model domain and moves in negative x-direction. Its advance commences 20,000 years after the transition to the cold period and takes another 20,000 years until the glacier has fully developed and the maximum height and extension are reached. Upon transition to the next warm phase, the glacier shrinks linearly until it has fully receded when the transition is over. This simplified glacial cycle could repeat afterwards, however this study focuses on only one cycle, as this proved sufficient to gather all major insights.

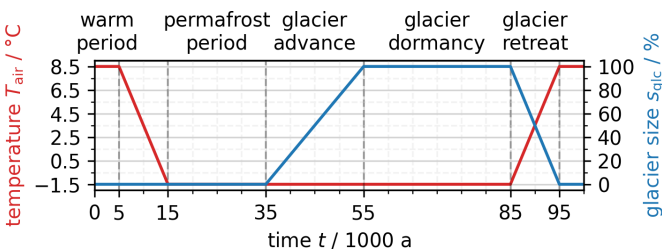


**Figure 3.** Temporal evolution of surface temperature and glacier size during glacial cycles

As done in other studies [Bea et al., 2018, Bense and Person, 2008, Nasir et al., 2011, Rühaak et al., 2014], a

simplified analytical model is used here to describe the glacier. As proposed in Van der Veen [2013], the time and location-dependent height of the glacier  $h(t, x)$  is defined as in Equation 5. The maximum height of the glacier  $h_{\text{max}}$  is set to 700 m and the maximum lateral extension  $L_{\text{max}}$  to 80 % of the model's width.  $x_0$  is the horizontal coordinate of the domain's right boundary and  $s_{\text{glc}}$  the scaling factor for the glacier size.

$$h(t, x) = \begin{cases} h_{\text{max}} s_{\text{glc}}(t) \left(1 - \left(\frac{x_0 - x}{L_{\text{max}} s_{\text{glc}}(t)}\right)^{2.5}\right)^{1.5} & , \text{if } s_{\text{glc}}(t) > 0 \\ 0 & , \text{otherwise.} \end{cases} \quad (5)$$

The presence of the glacier influences the boundary conditions for all three simulated physical processes. An overview for all boundary conditions is shown in Table 1. Thermally, the parts of the top boundary covered by the glacier are fixed to a constant glacier bed temperature of  $T_g = 0.5^\circ\text{C}$ . That is due to the assumption of a temperate ("warm") or wet-based glacier where the entire bed is at the pressure-melting point [Hambrey and Glasser, 2012]. The uncovered parts of the surface adhere to the temperature profile in Figure 3. To avoid a numerically undesirable jump in values, for a transition length of  $l_t = 200\text{m}$  in front of the glacier the temperature is interpolated with a smoothstep function:  $T_{\text{top}} = T_{\text{air}} + (T_g - T_{\text{air}}) \xi^2 (3 - 2\xi)$  with  $\xi = \min(\max(1 + (x - x_g)/l_t, 0), 1)$ , where  $x_g$  is the horizontal coordinate of the glacier tip. Hydraulically, the glacier imposes a fluid pressure, which is proportional to the glacier's height and the ice density. Water pressure at glacier beds matching this relation have been reported [Hart et al., 2022]. It is questionable however, whether the hydraulic pressure would remain at that level over time, while also discharging into the ground. Thus, the glacier-induced groundwater influx is likely consistently (and conservatively) overestimated in this study. The glacier induced pore pressure  $p_{\text{glc}}$  also adds to the hydrostatic pore pressure distribution  $p_{\text{hs}}$  at the

right boundary; they are defined as

$$p_{\text{glc}} = \rho_{\text{ice}} g h(t, x) \quad \text{and} \quad (6)$$

$$p_{\text{hs}} = [\exp(\beta_{pF} \rho_{\text{water}} g \Delta y) - 1] / \beta_{pF} \quad (7)$$

with  $\rho_{\text{ice}} = 900 \text{ kg m}^{-3}$ ,  $\rho_{\text{water}} = 1000 \text{ kg m}^{-3}$ ,  $g = 9.81 \text{ m s}^{-2}$ , the fluid compressibility  $\beta_{pF} = 5 \cdot 10^{-10} \text{ Pa}^{-1}$  and  $\Delta y$  being the depth below surface. The exponential hydrostatic pressure profile results from the pressure dependency of the water density (see Table 4).

Mechanically, the gravitational load of the glacier acts on the top boundary of the model and governs the vertical stresses. The remaining constants used in the boundary conditions are: the geothermal heat flux  $q_{\text{geo}} = 65 \text{ mW m}^{-2}$  and the atmospheric pressure  $p_{\text{atm}} = 0.1 \text{ MPa}$ . In this study, the simulations were run with all different process couplings (i.e. T, H, M, TH, TM, HM, THM) for better understanding of the occurring phenomena.

### 3.3. Repository source term

The repository is geometrically represented as a line on which a heat source with exponential decay is applied. A conservative proxy model "DWR-Mix 89/11" as described in the GRS RESUS reports [Bertrams et al., 2020] is used to model the heat production, using four artificial leading radionuclides to represent nuclear decay over a period of one million years. The generated heat can be described as

$$Q = \sum_{n=1}^{N^*} \sum_{i=1}^4 Q_i \exp\left[-\ln(2) \frac{t^*}{\tau_i}\right] \quad \text{with} \quad (8)$$

$$t^* = t - (n/N) t_{\text{deposit}} + t_{\text{interim}} \quad \text{and}$$

$$N^* = \min(t/t_{\text{deposit}}, 1) N.$$

This equation accounts for the decay during interim storage ( $t_{\text{interim}} = 57 \text{ a}$ ) and during deposition of the waste ( $t_{\text{deposit}} = 30 \text{ a}$ ). The half-life times  $\tau_i$  and the heat generated by each leading radionuclide per nuclear waste bundle  $q_i$  are given in Table 2. Following the data in Bertrams et al. [2020], the total number of nuclear waste bundles deposited in the repository amounts to  $N = 34,630$ . Figure 4 shows the heat output of this model and for each nuclide over time. For the simulation, the time-dependent heat is prescribed as a source term on a central horizontal section of the model within the z2NA geological horizon. The repository is located at a depth of approximately  $-850 \text{ m}$  and has a length of  $1.33 \text{ km}$  (representing a flat area of  $1.8 \text{ km}^2$ ).

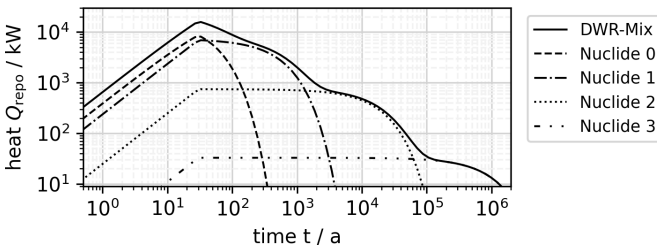


**Figure 4.** Heat evolution of nuclear waste repository for the "DWR-Mix 89/11" model

### 3.4. Material models

Similar studies [Lang and Hampel, 2023, Lang et al., 2014] have simplified their material models to linear viscosity, reasoning that pressure-solution creep dominates on long time scales. To capture the pressure-solution creep as well as the dislocation creep, we represent the viscoelastic mechanical behavior of rock salt by using an established composite power law model [Marketos et al., 2016, Spiers and Carter, 1998, Urai and Spiers, 2017]. It is defined by the equivalent creep strain rate

$$\dot{\epsilon}^{\text{cr}} = A \exp\left(-\frac{Q}{RT}\right) \left(\frac{\sigma_v}{\sigma_f}\right)^n + \frac{A_2}{D^3 T} \exp\left(-\frac{Q_2}{RT}\right) \frac{\sigma_v}{\sigma_f} \quad (9)$$

with  $\sigma_v$  being the von-Mises equivalent stress, which can be calculated with the principal stresses  $\sigma_i$  as

$$\sigma_v = \sqrt{\frac{1}{2} ((\sigma_1 - \sigma_2)^2 + (\sigma_2 - \sigma_3)^2 + (\sigma_3 - \sigma_1)^2)}. \quad (10)$$

The two components account for dislocation creep and pressure-solution creep, respectively. The latter term is dominating the creep law at low von-Mises equivalent stresses due to the exponent  $n$ . Both terms are dependent on the temperature  $T$ . The pressure-solution creep also depends on the grain size  $D$ , which is set to a constant here, assuming a homogeneous distribution within the salt layers. The parameters used in this study can be found in Table 3. For the power law term they are the same as in the stationary creep model called BGRa in Hunsche and Schulze [1994]. For the linear term, the activation energy  $Q_2$  was taken as determined in Spiers et al. [1990]. The remaining parameters were fitted by Zill et al. [2022] to better match experimental data of creep tests at low deviatoric stresses, as it was done in Bérest et al. [2019]. Table 5 shows, which layers use this creep model. The remaining layers are modelled with linear elasticity.

### 3.5. Initial State

To get meaningful initial states for the main simulations, initial simulations are run until a steady state is reached. Therein, the same boundary conditions are used as in Table 1, with the exception of omitting the nuclear waste heat and the glacial cycles. Thus, for each main simulation per process coupling a corresponding initial state is computed. For the mechanical related processes, the displacement field is reset to zero, while keeping the equilibrated stress field.

### 3.6. Hydraulic deactivation of rock salt

The simulation framework employed in this study is designed to solve for Darcy flow within fully saturated porous media across the entire domain. However, the extremely low permeability of rock salt poses a challenge. We assume an undamaged state of the salt layers in the bedded formation present here. Consequently, the entire rock salt strata can be considered hydraulically tight. To avoid nonphysical parameter values chosen only to mimic impermeable rock, which would also be prone to numerical oscillations or instabilities, the hydraulic component in the system of equations was deactivated for all layers below z5. As a result, only the

upper three layers are considered porous media and exhibit fluid flow in the simulations. In other words, we solve a TM-coupled problem for the saline layers and a THM problem for the porous rocks.

### 3.7. Stabilization

The presence of advection-diffusion instabilities in the Finite Element Method is a well-known phenomenon [Masud and Khurram, 2004]. Given that the boundary conditions employed in this study permit high fluid velocities, which can trigger these instabilities, addressing them is essential. To mitigate such instabilities while maintaining computational efficiency, a simple isotropic diffusion stabilization method was employed for this study. This stabilization scheme adds an adjustable artificial isotropic balancing dissipation to the thermal diffusion coefficient. It is defined as

$$\mathbf{K}_\delta = \frac{1}{2} a \|\mathbf{v}\| h \mathbf{I} \quad (11)$$

with  $\mathbf{v}$  being the Darcy velocity,  $h$  being the element size (maximum edge length) and  $\mathbf{I}$  the identity matrix. The tuning parameter  $a$  was kept at 1. The applied stabilization scheme was validated with benchmarks to ensure that they do not compromise the accuracy or validity of the numerical solution [Bilke et al., 2019, 2024].

### 3.8. Numerical settings

The simulations presented in this study were performed using the FEM with a monolithic coupling approach. We utilized a Newton non-linear solver alongside backward Euler time discretization. The absolute tolerances of the Euclidian norm were set to  $10^{-3}$  K, 0.02 Pa and  $10^{-6}$  m for the temperature, pressure and displacement components respectively. The linear solver employed the Pardiso LU factorization with scaling enabled. For the time stepping, a sequence of 40 steps each 2.5 a, 36 steps each 25 a and steps of 500 a thereafter was applied.

## 4. Results

Evaluation of the simulation results begins with an examination of the initial states, providing a baseline for subsequent analysis. Following this, transient simulations are inspected to evaluate the different process couplings and dynamics at play.

### 4.1. Initial steady state simulations

The initial temperature field (Figure 10) is shaped by the steady-state groundwater flow (Figure 11). Topography-driven groundwater currents transport heat from lower layers to the surface, which can be observed in the form of two vertical plumes that extend nearly to the surface. This also leads to varying – and overall shallower – vertical temperature gradients across the domain. Simulations with an uncoupled T process show a maximum temperature which is roughly 20 K higher than in the TH coupled case. The velocity magnitudes of the steady state flow correlate to slopes on the domain's surface and agree qualitatively with analytical solutions of analogous problems [Toth, 1963].

In the equilibrated initial stress field the salt layers significantly disrupt the otherwise lithostatic stress profile. This is due to the deviatoric stress relief via creep in the salt layers, resulting in an isotropic stress state. Figure 12 shows the von-Mises equivalent stress to highlight this state. It is clearly visible, that the rock salt strata are divided into two separate domains. This is caused by the z3HA layer, which is modeled with linear elasticity. In the salt layers, the deviatoric stress is multiple magnitudes lower compared to the other layers.

### 4.2. Main simulations

With the initial states from the preceding stage, the main simulations including the glacial cycles and nuclear waste heat were performed for the different possible process coupling schemes.

#### 4.2.1. Thermal maximum

First, we examine the change in temperature as a consequence of the decay heat in the nuclear waste repository. The left half of Figure 5 shows the temperature field at the thermal maximum at the DGR, which is 800 years into the TH/THM simulation.

The highest temperature in the center of the repository reaches 101.6 °C. At the same time the edge of the repository exhibits temperatures as low as 70 °C. The deviation from the initial steady state temperature field extends roughly 500 m laterally of the repository and quickly diminishes upon reaching the aquifers in vertical direction. For comparison, without the hydraulic coupling (T, TM) a maximum temperature of 113.3 °C is reached at 825 years. We need to emphasize, that the temperatures resulting from the employed 2D models are overestimated, because of lower potential for heat dissipation than in three spatial dimensions.

In the models including thermo-mechanical coupling (TM, THM), the increase in temperature causes thermal expansion in the corresponding part of the domain. The right half of Figure 5 displays the resulting displacement magnitudes at the thermal maximum of the THM simulation with lines indicating the displacement vector directions.

At the peak, the domain is lifted by 2.246 m centered above the repository close to the surface. The rest of the domain is displaced – to a much lesser extend – partly laterally outwards and partly upwards. This uplift occurs due to the thermal expansivity of the geological layers, which is high for most of the salt layers (see Table 5). At this stage of the simulation, the hydraulic state of the model is basically identical to the initial state, as the slight elevation and increased temperatures do not significantly change the pressure profile.

For comprehensive illustration of the thermal behavior during the glacial cycle, the temperature data is probed along a vertical line centered on the repository through all timesteps. The resulting contour plot over depth and time is shown in Figure 6 for the T model on the left and for the TH model on the right. The corresponding models with mechanical coupling do not contain noticeable deviations to this data.

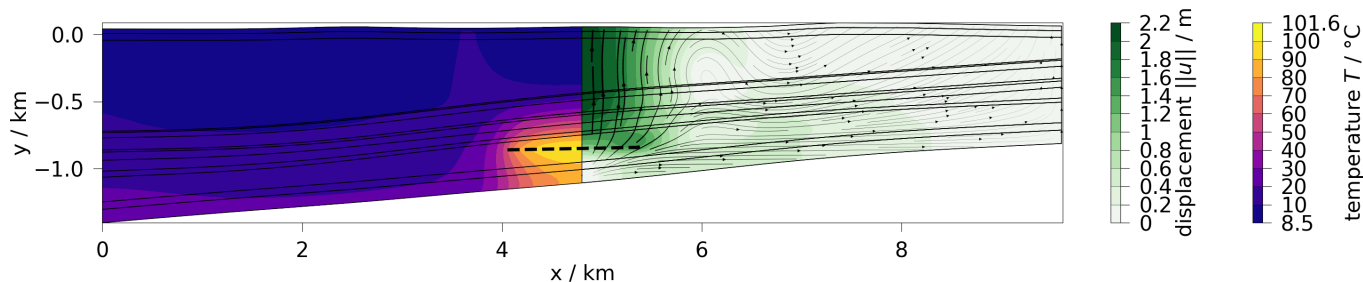


**Figure 5.** Temperature and displacement field at thermal maximum ( $t = 800$  a) of the THM simulation

This visualization helps to evaluate the effect of the groundwater flow in the top layers on the temperature evolution in the entire domain. Due to the high fluid velocities in the upper layers, the groundwater currents advect heat away at a very high rate, which has multiple implications. The thermal deviation caused by DGR heat reaches the top surface for the T model, but not for TH model, because the heat is removed faster than it can accumulate. Further, elevated temperatures persist longer without the hydraulic coupling. As the model does not include the phase change of water upon freezing, fluid influx from the surface is still occurring during permafrost. This causes the permafrost to spread all the way down to the interface with the hydraulically deactivated salt layers. The flow field at the end of the glacier dormancy, is predominated by the glacier induced hydraulic overhead, resulting in a circulation flow from the right side of the domain to the left.

#### 4.2.2. Mechanical response to glacial overburden

Figures 7 and 8 show the displacement field and the von-Mises stress field at the end of the glacial dormancy phase. For visual purposes, the glacier is scaled down by 50%. The right side of the model is being compressed under the weight of the glacier. The salt layers exhibit a significant amount of displacement via creep due to the overburden, separated by the elastically modelled z3HA layer. Due to the vast amount of material displacing towards the left, the above layers lift slightly. Importantly, the displacement field concentrates towards a small range in the center of the model. This likely implies that the extend of the model is too small to avoid boundary effects influencing the area of interest, in this case the DGR in the center. Investigating

the von-Mises stress field, we can observe lowered values in the salt layers. This means, the salt layers would continue to release deviatoric stress via creep even though the boundary conditions stayed the same for 30,000 years. The stress state of the salt strata can be readily evaluated in terms of integrity criteria. Both the fluid pressure criterion and the dilatancy criterion were not violated during the simulation. Further insight is provided in Appendix D with exemplary illustrations and more detailed information.

#### 4.2.3. Influence of process coupling

In this section, the thermal and mechanical development in the DGR in response to the heat generated inside and the transient boundary conditions is evaluated. Figure 9 shows the temperature, displacement and von-Mises stress at the DGR over the duration of one glacial cycle. Each solid line stands for the respective values at the DGR center, whereas the corresponding filled areas portrait the range of values which occur throughout the entire length of the DGR. For comparison, the plots contain the different simulated processes with individual coloring.

Inspecting the temperature evolution, we can observe a wide range of values during the initial heating, followed by a rapid decline. The hydraulic coupling results in a quicker decrease and a lower minimum temperature. The mechanical coupling has no influence on the temperature evolution. At the end of the glacial cycle, the heat of the DGR has mostly dissipated and the temperatures increase again due to the starting warm period.

Analyzing the displacement, the DGR initially lifts vertically and expands horizontally in both directions for the models containing thermal coupling. Afterwards, it settles

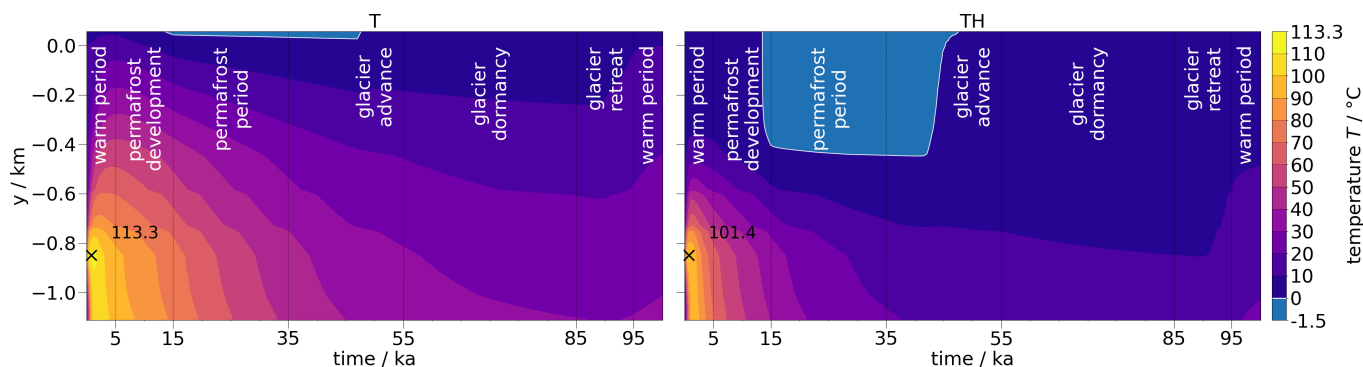


**Figure 6.** Temperature evolution along vertical line through center of DGR for T- (left) and TH- (right) simulations

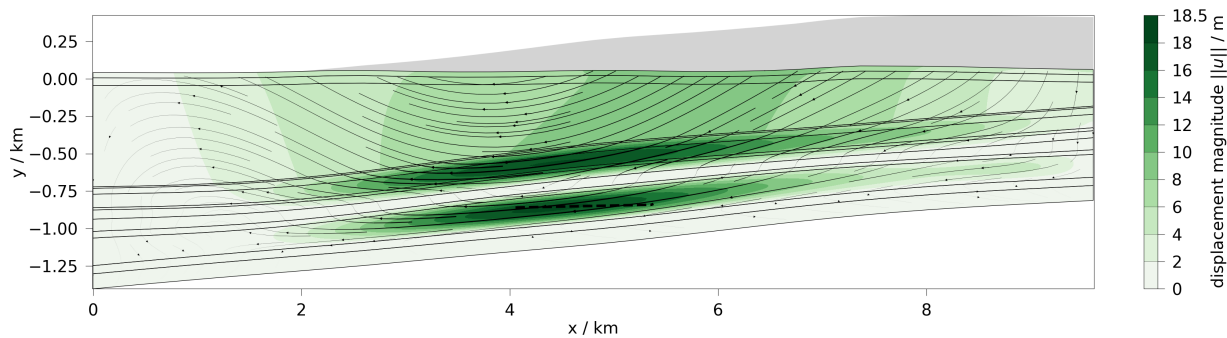


**Figure 7.** Displacement field at the end of glacial dormancy ( $t = 85\,000$  a) of the THM simulation

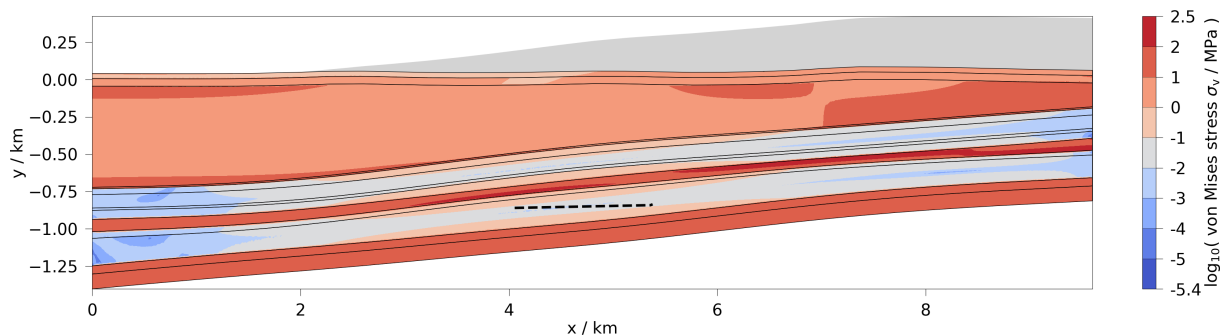


**Figure 8.** Log-scaled von-Mises equivalent stress field at the end of glacial dormancy ( $t = 85\,000$  a) of the THM simulation

fastest for the THM model due to the rapid cooling provided by the advective heat transport. After the glacier stops advancing, there is a steady creep that occurs both horizontally and vertically, with the horizontal displacement being more pronounced. However, as the glacier begins to retreat, the direction of creep reverses and there is a partial reduction in the accumulated displacement.

The creep rates of the models, in order of magnitude, are as follows: THM < HM < TM < M. This trend can be attributed to the temperature dependence inherent in the creep model. Lower temperatures correlate with lower creep rates. As a consequence, in the hydraulically coupled models, where advective heat transport reduces the temperatures in the salt layers, a correspondingly lower creep potential is observed.

The introduction of thermal coupling further reduces the creep rate. This reduction occurs because models without thermal coupling rely on the initial state temperature as a constant reference during the glaciation phase of the simulation. Models with thermal coupling have reduced temperatures within the salt layers.

Significant shear strains are induced at the interface with adjacent rocks due to the large creep displacements within the salt layers. Future runs should include interface elements and finite strain formulations to improve the accuracy of the representation to better capture these conditions.

We can further observe, that the von-Mises stress maximum is at the very beginning, where heat generated by the DGR is highest. The accompanying thermomechanical stresses are reflected in the von-Mises stress and are quickly

released thereafter. It is followed by generally low levels with the minimum being just prior to the glacier advance. Upon glacier advance and retreat there is a complex alternation of stress increase and decrease. This is caused by regions of differing von-Mises stresses, which travel through the salt layers, synchronous with the glacier movement. During glacier dormancy, the stress is about one order of magnitude higher compared to the pre-glacial state.

## 5. Conclusion

Large-scale models are a fundamental tool for the assessment of the long-term stability, integrity and safety of salt formations in a wide range of engineering applications. A significant advancement in research efficiency and quality is the automation of simulation workflows, which streamlines the process of concatenating the individual steps in pre-processing, model execution and post-processing [Lehmann et al., 2024]. This capability allows for a comprehensive exploration of the parameter space, improves understanding of the problem under investigation, and allows for rapid testing of different model setups. The results provide a comprehensive benchmark for systematically improving models and investigating more complex physical phenomena.

A notable insight from the simulation results is that due to the simplified nature of the geometric model, boundary conditions can have a significant impact on the results within the central region of interest. Extending the scope of the model is a straightforward solution. However, it comes

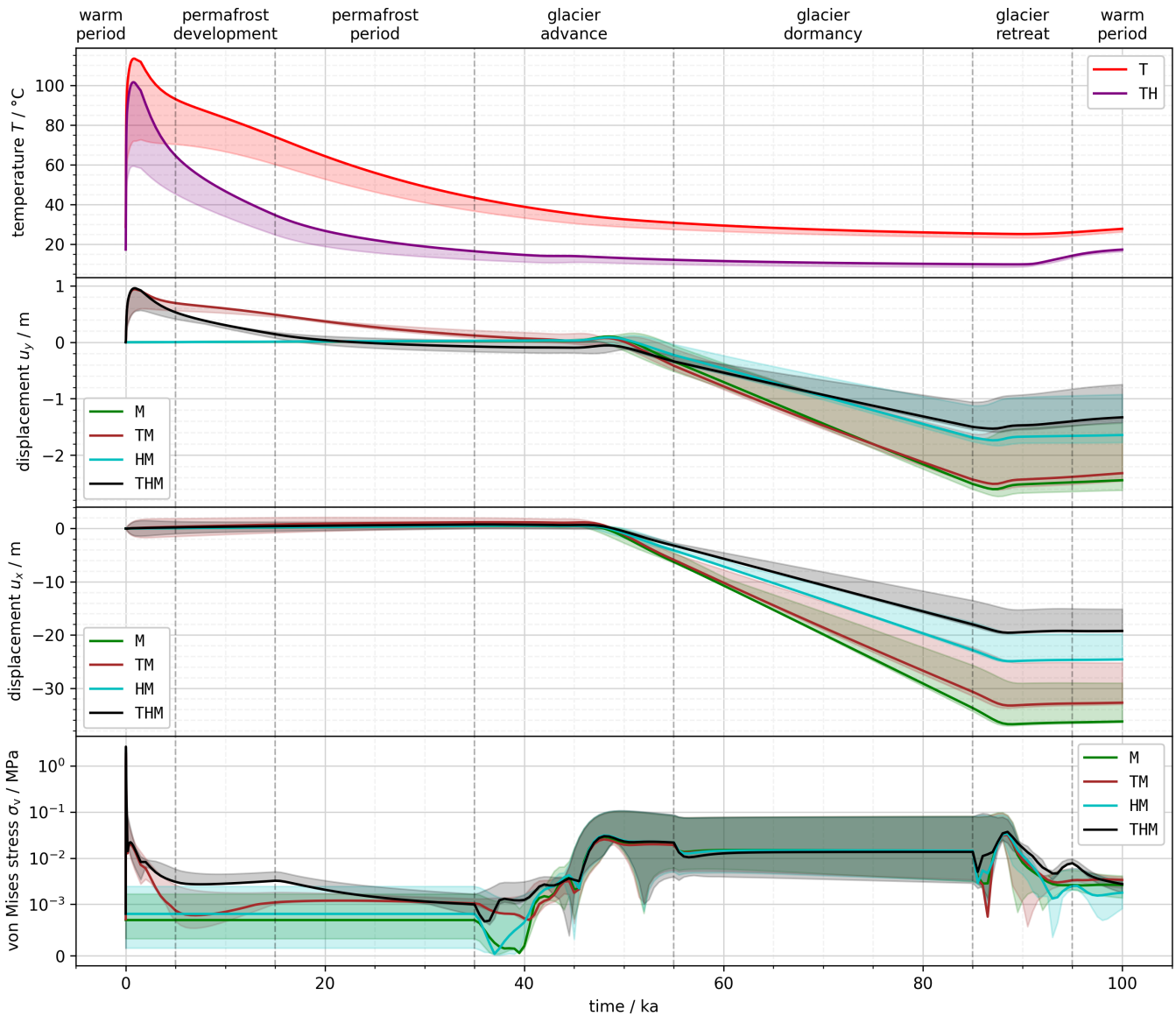


**Figure 9.** Comparison of the different process couplings for the temporal evolution of temperature, displacement and von-Mises stress in the DGR (solid line: repository center, area: range of values along the repository)

at the cost of increased computational complexity. In addition, the limited availability of geological data may place constraints on model extension.

Our results emphasize the significant role that hydraulic boundary conditions play in the shaping of the results. The advective heat transport influenced by these conditions exerts a significant influence on the temperature field. This in turn affects the mechanical response of the system. The influence of advective heat transport may be overestimated in the results presented, given the assumption of fully saturated porous media and the conservative hydraulic head induced by the glacier. If near-surface processes (e.g. overconsolidation, erosion, flow patterns) are of interest, a better representation of permafrost as well as plastic material models in the top layers should be applied.

Regarding the temperature evolution at the DGR, the simplified 2D models employed in this study are in a sense more conservative as a 3D model, as the decay heat has

one dimension less to dissipate into. A full 3D model is desirable nonetheless for more accurate results and to provide boundary conditions for more complex near field simulations.

## Conflicts of Interest

The authors declare that they have no known competing financial interests or personal relationships that could have appeared to influence the work reported in this article. The complete review history is available online.

## Acknowledgements

This research was funded by the Federal Office for the Safety of Nuclear Waste Management (BASE) under Grant No. 4719F10402 (AREHS project). We thank the OGS developers, especially Dr. Dmitri Naumov and Dr. Wenqing Wang for their valuable support.

## Appendix A. Initial state

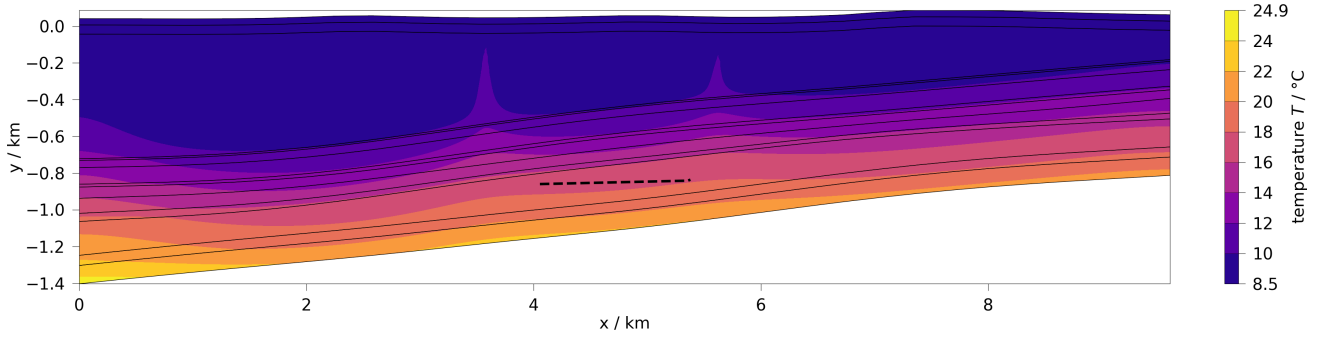


Figure 10. Initial steady-state temperature field for THM model

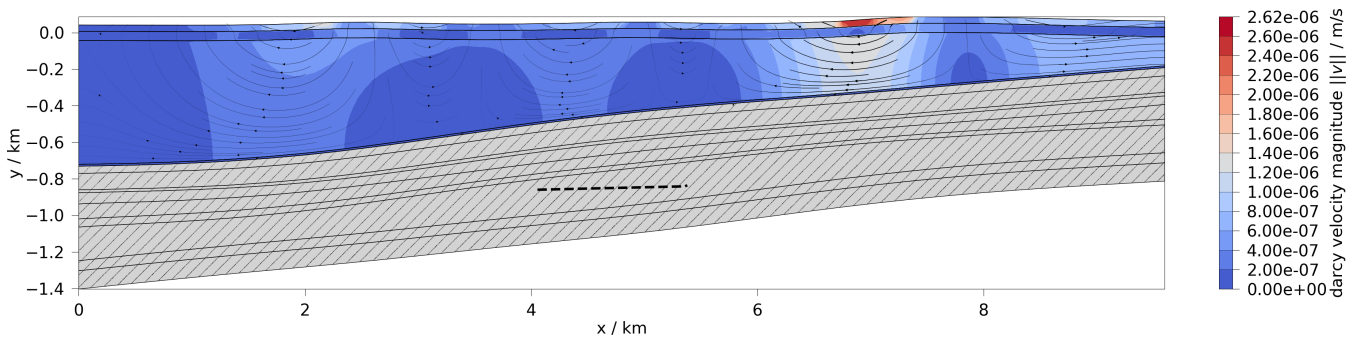


Figure 11. Initial steady-state velocity field for THM model

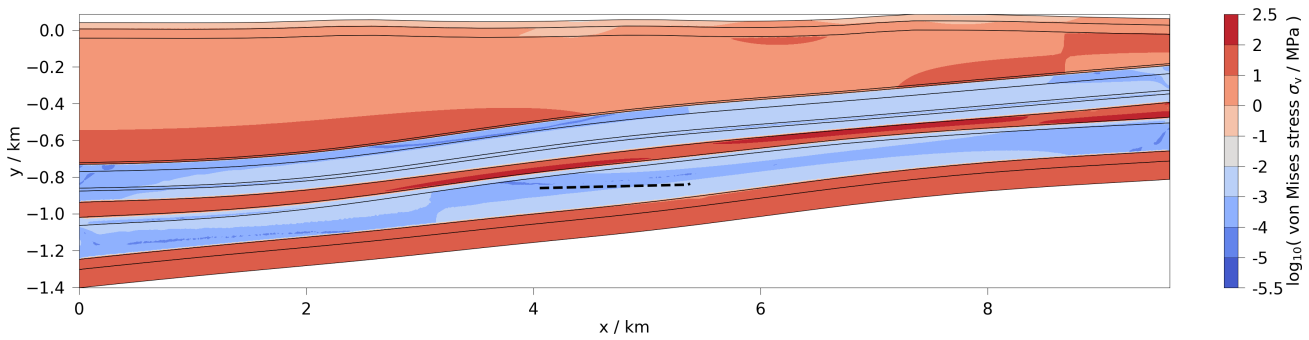
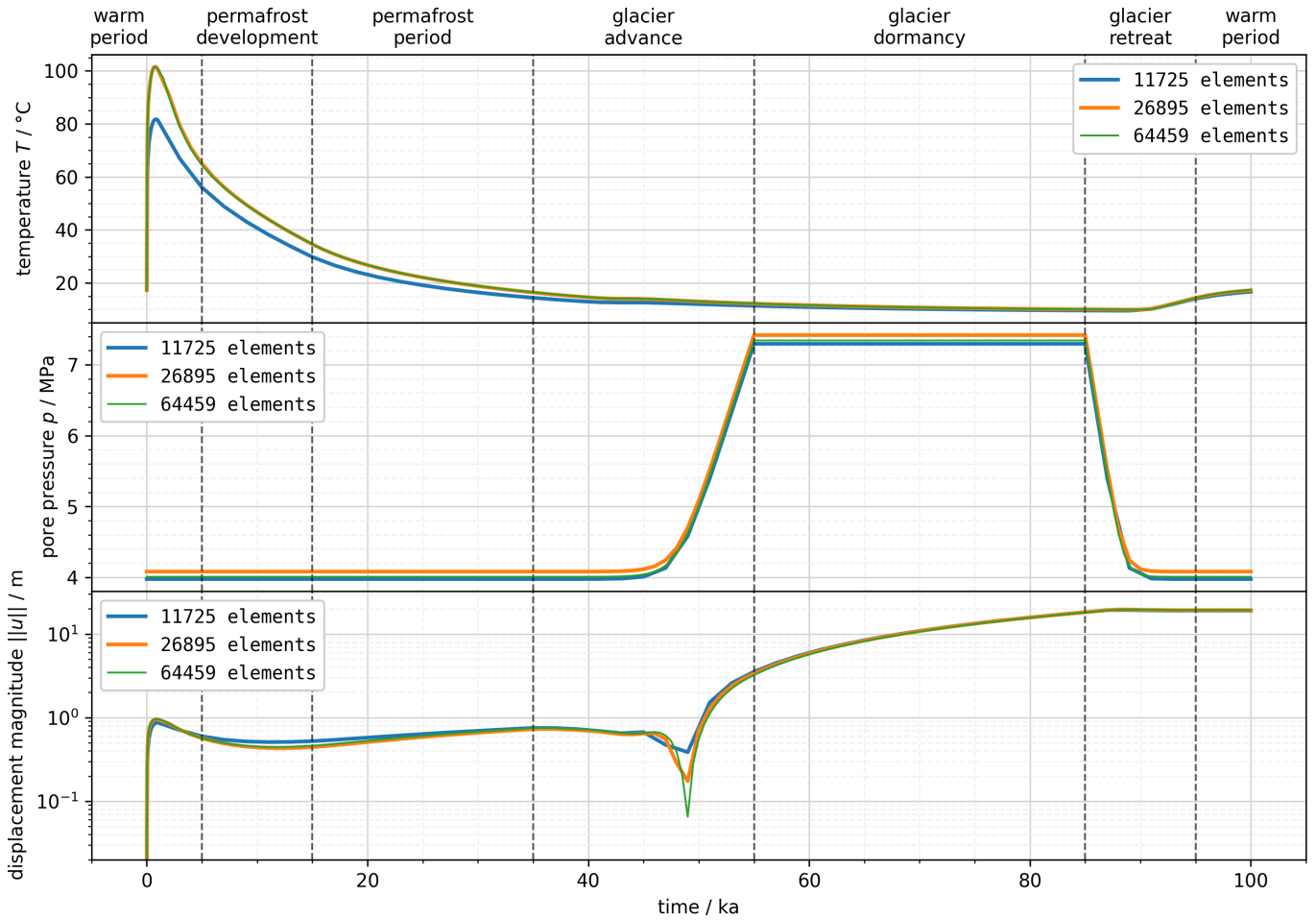


Figure 12. Initial steady-state von-Mises equivalent stress field for THM model

## Appendix B. Convergence behavior



**Figure 13.** Comparison of THM-results for three different discretizations; temperature and displacement measured at repository center, pore pressure measured 500 m above repository center

To test our model for convergence we simulated three different discretizations:

- 64 459 elements: 40 x 2.5 a, 36 x 25 a, 500 a thereafter
- 26 895 elements: 20 x 5 a, 18 x 50 a, 1000 a thereafter
- 11 725 elements: 10 x 10 a, 9 x 100 a, 2000 a thereafter

In Figure 13 a comparison of the evolution of the three process variables temperature, pore pressure and displacement for THM simulations with the aforementioned discretizations is presented. Displacement and pore pressure are measured at the repository center. Due to the hydraulic deactivation, the pore pressure is measured 500 m above that point. The coarsest discretization shows significantly lower temperatures as the finer discretizations, which match very closely. The pore pressure is not significantly affected by the changing discretization. The same is true for the displacement evolution with an exception of a short period during the glacier advance, where the displacement magnitude is getting increasingly smaller with finer discretization. Overall it can be expected, that the simulation results of the finest discretization will not change significantly with further refinement of the discretization.

## Appendix C. Considerations regarding non-linear behavior of the fluid phase

Permafrost can reduce the permeability of saturated soils by several orders of magnitude [Jin et al., 2022]. However, incorporation of such a temperature-dependent permeability would significantly influence the flow patterns. This would change the hydraulic behaviour at the top layers and, via process coupling, also the heat transport and the mechanical response. However, permeability changes over orders of magnitude are a significant source of non-linearity and pose challenges for numerical convergence. One approach to mitigate this issue is using an adaptive mesh refinement as it was done by Rühaak et al. [2015] and Grenier et al. [2018]. As the localized evolution of the permafrost layer through freezing and thawing was not the primary focus of this study, this feature was not included. We did however test a boundary condition approach, which mimics this behavior: the boundary condition at the top surface for the hydraulic pressure can be applied only when the temperature is above the freezing point, otherwise we apply a no-flow (closed) boundary condition. This effectively removed all topography driven groundwater currents upon reaching the permafrost phase. Instead, a horizontally dominated flow field from the right to the left boundary formed, which drastically reduced the vertical heat transport. As a consequence, the permafrost did not reach the rock salt strata at maximum extent anymore, but approximately 30 m deep. In the depths of the DGR the temperatures at glacier dormancy are 10 K to 20 K lower, but there is no visible impact on the mechanical response of the repository. This approach might be useful to achieve similar behavior as a model including temperature-dependent permeability, without sacrificing performance. However, a flow concentration forms at the interface between the glacially covered and uncovered part of the top surface. This non-conformity in the boundary condition might require additional modeling techniques.

Another non-linear aspect which was tested in this study is the latent heat associated with the phase change of water. It was not incorporated into the model, because our tests indicated that its exclusion did not exert a significant influence on the results at the time scale considered.

While pressure-dependence was included for the water density in this study (see table 4), temperature dependence was omitted. Its inclusion would have resulted in convection cells, which presumably would not have altered the model behavior significantly, but taken a toll on the numerical performance.

## Appendix D. Evaluation of integrity criteria

As was done by Li et al. [2022] for salt caverns, we can analyze integrity criteria to further evaluate the simulation results. The fluid pressure criterion reads as

$$F_p = p - \sigma_{\min} < 0 \quad (12)$$

with  $\sigma_{\min}$  being the least compressive principal stress (compression positive) and  $p$  being the fluid pressure. As the salt layers are hydraulically deactivated in our models we employ a hypothetical depth dependent water column for the fluid pressure. The dilatancy criterion [Cristescu and Hunsche, 1998] in total stress formulation is given as

$$F_{\text{dilat}} = \frac{\tau_{\text{oct}}}{\sigma_0} - a \left( \frac{\sigma_m}{\sigma_0} \right)^2 - b \frac{\sigma_m}{\sigma_0} < 0 \quad (13)$$

with  $\tau_{\text{oct}}$  being the octahedral shear stress,  $\sigma_m$  being the mean stress,  $\sigma_0 = 1 \text{ MPa}$  and the parameters  $a = 0.0123$  and  $b = 0.7731$  are the same as in Ma et al. [2015] and Li et al. [2022]. The evaluation is limited to the rock salt strata. Figures 14 and 15 show both criteria evaluated for the THM simulation at the end of the glacier dormancy. It can be seen that both criteria hold true as they are below zero. Thus - under the present conditions and assumptions of this generic model - integrity criteria are met, though it has to be noted, that the model still lacks relevant features for a safety assessment.

## Appendix E. Parameters

**Table 2.** Thermal output per waste bundle and half-life times per leading nuclide [Bertrams et al., 2020]

| i                       | 1     | 2     | 3     | 4      |
|-------------------------|-------|-------|-------|--------|
| $q_i / \text{W}$        | 1156  | 226.7 | 21.51 | 0.9466 |
| $\tau_i / \text{years}$ | 32.20 | 396.8 | 13670 | 759300 |

The following thermal conductivity model is used:

$$\lambda_{\text{total}} = \lambda_{\text{LR}} \phi + \lambda_{\text{S}} (1 - \phi) \quad (14)$$

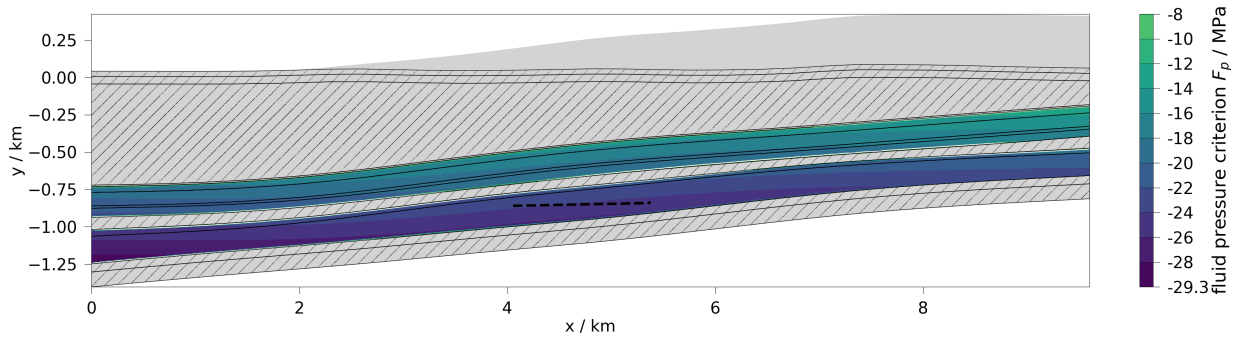


**Figure 14.** Fluid pressure criterion at the end of glacial dormancy ( $t = 85\,000$  a) of the THM simulation

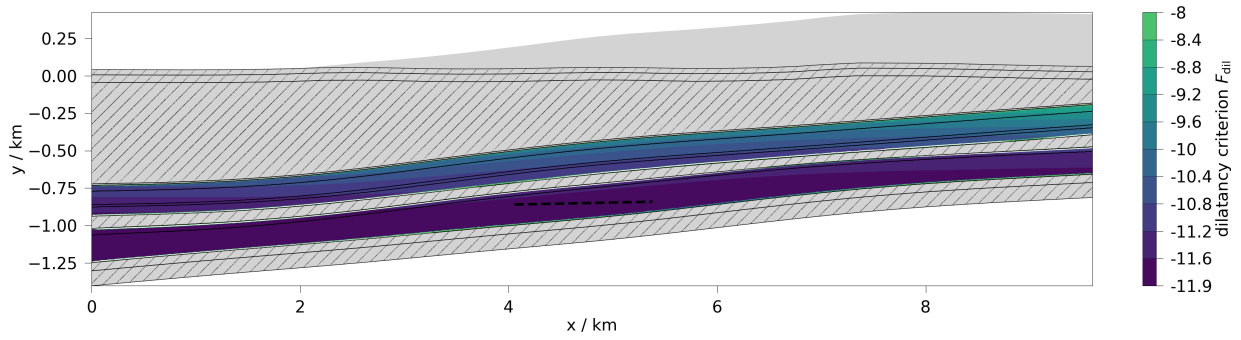


**Figure 15.** Dilatancy criterion at the end of glacial dormancy ( $t = 85\,000$  a) of the THM simulation

**Table 3.** Viscoelastic creep law parameters

|        | reference stress | universal gas constant           | exponent | grain size | parameter       | parameter                   | activation energy    | activation energy    |
|--------|------------------|----------------------------------|----------|------------|-----------------|-----------------------------|----------------------|----------------------|
| symbol | $\sigma_f$       | $R$                              | $n$      | $D$        | $A$             | $A_2$                       | $Q$                  | $Q_2$                |
| unit   | MPa              | $\text{JK}^{-1} \text{mol}^{-1}$ | -        | cm         | $\text{d}^{-1}$ | $\text{m}^3 \text{Kd}^{-1}$ | $\text{kJ mol}^{-1}$ | $\text{kJ mol}^{-1}$ |
| value  | 1                | 8.314462                         | 5        | 5          | 0.18            | $6.5 \cdot 10^{-10}$        | 54                   | 24.5                 |

**Table 4.** Liquid properties

|        | density   | compressibility     | Specific heat capacity          | Thermal expansivity  | Thermal conductivity           | viscosity         |
|--------|---|---------------------|---------------------------------|----------------------|--------------------------------|-------------------|
| symbol | $\rho_{\text{FR}}$                                  | $\beta_{p\text{F}}$ | $c_{p\text{F}}$                 | $\beta_{T\text{F}}$  | $\lambda_{\text{F}}$           | $\mu_{\text{FR}}$ |
| unit   | $\text{kgm}^{-3}$                                   | $\text{Pa}^{-1}$    | $\text{Jkg}^{-1} \text{K}^{-1}$ | $\text{K}^{-1}$      | $\text{Wm}^{-1} \text{K}^{-1}$ | Pas               |
| value  | $1000(1 + \beta_{p\text{F}}(p - p_{\text{ref}}^*))$ | $5 \cdot 10^{-10}$  | 4280                            | $25.7 \cdot 10^{-5}$ | 0.6                            | $10^{-3}$         |

\*  $p_{\text{ref}} = 0.1 \text{ MPa}$

**Table 5.** Material properties

|        | Formation           | Solid density     | Young's modulus | Poisson's ratio | Specific heat capacity         | Linear thermal expansivity | Thermal conductivity          | Porosity | Intrinsic permeability | Biot-Willis coefficient |
|--------|---------------------|-------------------|-----------------|-----------------|--------------------------------|----------------------------|-------------------------------|----------|------------------------|-------------------------|
| symbol |                     | $\rho_{SR}$       | $E$             | $\nu$           | $c_{pS}$                       | $\alpha_{TS}$              | $\lambda_S$                   | $\phi$   | $k$                    | $\alpha_B$              |
| unit   |                     | $\text{kgm}^{-3}$ | GPa             | -               | $\text{Jkg}^{-1}\text{K}^{-1}$ | $10^{-5}/\text{K}$         | $\text{Wm}^{-1}\text{K}^{-1}$ | -        | $\text{m}^2$           | -                       |
| q      | Quaternary          | 2500              | 0.1             | 0.33            | 950                            | 1                          | 2.3                           | 0.2      | $5.5 \cdot 10^{-12}$   | 0.6                     |
| t      | Tertiary            | 2300              | 0.5             | 0.33            | 910                            | 1                          | 2.1                           | 0.1      | $5.05 \cdot 10^{-13}$  | 0.6                     |
| sm-su  | Buntsandstein       | 2700              | 1.5             | 0.27            | 760                            | 1                          | 2.6                           | 0.15     | $5.5 \cdot 10^{-12}$   | 0.5                     |
| z5     | Ohre Sediments      | 2500              | 1.5             | 0.27            | 760                            | 1                          | 2.6                           | 0.0      | $10^{-21}$             | 0.0                     |
| z4NA*  | Aller Rock Salt     | 2235              | 25              | 0.27            | 860                            | 4                          | 4.54                          | -        | -                      | -                       |
| z3SS*  | Schwaden Salt       | 2275              | 30              | 0.27            | 860                            | 3.5                        | 4.54                          | -        | -                      | -                       |
| z3Ro*  | Kaliflöz Ronnenberg | 1850              | 16              | 0.26            | 900                            | 2.5                        | 1.5                           | -        | -                      | -                       |
| z3NA*  | Leine Rock Salt     | 2160              | 25              | 0.25            | 860                            | 4                          | 4.54                          | -        | -                      | -                       |
| z3HA   | Main Anhydrite      | 2700              | 60              | 0.25            | 860                            | 1.6                        | 4.2                           | -        | -                      | -                       |
| z2SF*  | Kaliflöz Staßfurt   | 1850              | 17              | 0.28            | 900                            | 2.5                        | 1.5                           | -        | -                      | -                       |
| z2NA*  | Staßfurt Rock Salt  | 2160              | 33              | 0.25            | 860                            | 4                          | 4.54                          | -        | -                      | -                       |
| z2BA   | Basal Anhydrite     | 2700              | 30              | 0.27            | 860                            | 1.6                        | 4.2                           | -        | -                      | -                       |
| ro     | Rotliegend          | 2700              | 17              | 0.27            | 760                            | 1                          | 2.7                           | -        | -                      | -                       |

\* These layers use the composite viscoelastic creep law.

The values are taken primarily from Bollingerfehr et al. [2018] and Bertrams et al. [2020]. Hydraulic properties are taken from Alfarrá et al. [2020].

## References

- Alfarra, A., Bertrams, N., and Bollingerfehr, W. (2020). Resus. Fundamentals for the evaluation of a repository system in a clay formation of greater thickness. Technical report, Gesellschaft fuer Anlagen-und Reaktorsicherheit (GRS) gGmbH.
- Bea, S. A., Su, D., Mayer, K. U., MacQuarrie, K. T., et al. (2018). Evaluation of the potential for dissolved oxygen ingress into deep sedimentary basins during a glaciation event. *Geofluids*, 2018.
- Bense, V. F. and Person, M. A. (2008). Transient hydrodynamics within intercratonic sedimentary basins during glacial cycles. *Journal of Geophysical Research: Earth Surface*, 113(4):1–17.
- Bérest, P., Gharbi, H., Brouard, B., Brückner, D., DeVries, K., Hévin, G., Hofer, G., Spiers, C., and Urai, J. (2019). Very slow creep tests on salt samples. *Rock Mechanics and Rock Engineering*, 52:2917–2934.
- Bertrams, N., Bollingerfehr, W., and Eickemeier, R. (2020). Resus. Fundamentals for the evaluation of a repository system in shallow salt formations. Technical report, Gesellschaft fuer Anlagen-und Reaktorsicherheit (GRS) gGmbH.
- Bilke, L., Flemisch, B., Kalbacher, T., Kolditz, O., Helmig, R., and Nagel, T. (2019). Development of Open-Source Porous Media Simulators: Principles and Experiences. *Transport in Porous Media*, 130(1):337–361.
- Bilke, L., Naumov, D., Wang, W., Fischer, T., Lehmann, C., Buchwald, J., Shao, H., Kiszkurko, F. K., Chen, C., Silbermann, C., Radeisen, E., Zill, F., Frieder, L., Kessler, K., and Ghasabeh, M. (2024). OpenGeoSys.
- Bollingerfehr, W., Bertrams, N., Buhmann, D., Eickemeier, R., Fahland, S., Filbert, W., Hammer, J., Kindlein, J., Knauth, M., Liu, W., et al. (2018). Kosina - Concept developments for a generic repository for heat-generating waste in bedded salt formations in Germany. *BGE TECHNOLOGY GmbH, BGE TEC*, 13.
- Bundesministerium für Umwelt, Naturschutz, nukleare Sicherheit und Verbraucherschutz (2023). Gesetz zur Suche und Auswahl eines Standortes für ein Endlager für hochradioaktive Abfälle (Standortauswahlgesetz - StandAG).
- Chen, J., Ren, S., Yang, C., Jiang, D., and Li, L. (2013). Self-healing characteristics of damaged rock salt under different healing conditions. *Materials*, 6(8):3438–3450.
- Cristescu, N. and Hunsche, U. (1998). *Time effects in rock mechanics*, volume 350. Wiley New York.
- Düsterloh, U. and Lux, K.-H. (2004). Geomechanical investigations into the hydraulic integrity of geological barriers. *International Journal of Rock Mechanics and Mining Sciences*, 41:286–291.
- Ehlers, W. and Wagner, A. (2019). Modelling and simulation methods applied to coupled problems in porous-media mechanics. *Archive of Applied Mechanics*, 89(4):609–628.
- Emiliani, C. (1955). Pleistocene temperatures. *The Journal of geology*, 63(6):538–578.
- Fischer, U. H., Bebiolka, A., Brandefelt, J., Cohen, D., Harper, J., Hirschorn, S., Jensen, M., Kennell, L., Liakka, J., Näs-lund, J.-O., et al. (2021). Radioactive waste under conditions of future ice ages. In *Snow and Ice-Related Hazards, Risks, and Disasters*, pages 323–375. Elsevier.
- Gloyna, E. F. and Reynolds, T. D. (1961). Permeability measurements of rock salt. *Journal of geophysical research*, 66(11):3913–3921.
- Gratier, J.-P., Dysthe, D. K., and Renard, F. (2013). The role of pressure solution creep in the ductility of the Earth's upper crust. *Advances in Geophysics*, 54:47–179.
- Grenier, C., Anbergen, H., Bense, V., Chanzy, Q., Coon, E., Collier, N., Costard, F., Ferry, M., Frampton, A., Frederick, J., et al. (2018). Groundwater flow and heat transport for systems undergoing freeze-thaw: Intercomparison of numerical simulators for 2D test cases. *Advances in Water Resources*, 114:196–218.
- Haerberli, W., Whiteman, C. A., and Shroder, J. F. (2021). *Snow and ice-related hazards, risks, and disasters*, volume 10. Elsevier.
- Hambrey, M. J. and Glasser, N. F. (2012). Discriminating glacier thermal and dynamic regimes in the sedimentary record. *Sedimentary Geology*, 251:1–33.
- Hardt, J., Dooley, T., and Hudec, M. (2023). Physical modeling of ice-sheet-induced salt movements using the example of northern Germany. *EGU sphere*, 2023:1–32.
- Hart, J. K., Young, D. S., Baurley, N. R., Robson, B. A., and Martinez, K. (2022). The seasonal evolution of subglacial drainage pathways beneath a soft-bedded glacier. *Communications Earth & Environment*, 3(1):1–13. Number: 1 Publisher: Nature Publishing Group.
- Hunsche, U. and Hampel, A. (1999). Rock salt—the mechanical properties of the host rock material for a radioactive waste repository. *Engineering Geology*, 52(3-4):271–291.
- Hunsche, U. and Schulze, O. (1994). Das Kriechverhalten von Steinsalz. *Kali und Steinsalz*, 11(8/9):238–255.
- Jin, H., Huang, Y., Bense, V. F., Ma, Q., Marchenko, S. S., Shepelev, V. V., Hu, Y., Liang, S., Spektor, V. V., Jin, X., Li, X., and Li, X. (2022). Permafrost Degradation and Its Hydrogeological Impacts. *Water*, 14(3):372. Number: 3 Publisher: Multidisciplinary Digital Publishing Institute.
- Jobmann, M., Bebiolka, A., Burlaka, V., Herold, P., Jahn, S., Lommerzheim, A., Maßmann, J., Meleshyn, A., Mrugalla, S., Reinhold, K., et al. (2017). Safety assessment methodology for a German high-level waste repository in clay formations. *Journal of Rock Mechanics and Geotechnical Engineering*, 9(5):856–876.
- Lang, J. and Hampel, A. (2023). Deformation of salt structures by ice-sheet loading: insights into the controlling parameters from numerical modelling. *International Journal of Earth Sciences*, 112(4):1133–1155.
- Lang, J., Hampel, A., Brandes, C., and Winsemann, J. (2014). Response of salt structures to ice-sheet loading: implications for ice-marginal and subglacial processes. *Quaternary Science Reviews*, 101:217–233.
- Lehmann, C., Bilke, L., Buchwald, J., Graebing, N., Grunwald, N., Heinze, J., Meisel, T., Lu, R., Naumov, D., Rink, K., Özgür Sen, O., Selzer, P., Shao, H., Wang, W., Zill, F., Nagel, T., and Kolditz, O. (2024). OpenWorkFlow—Development

- of an open-source synthesis-platform for safety investigations in the site selection process. *Grundwasser*, 29:31–47.
- Li, J., Zhang, N., Xu, W., Naumov, D., Fischer, T., Chen, Y., Zhuang, D., and Nagel, T. (2022). The influence of cavern length on deformation and barrier integrity around horizontal energy storage salt caverns. *Energy*, 244.
- Ma, H., Yang, C., Li, Y., Shi, X., Liu, J., and Wang, T. (2015). Stability evaluation of the underground gas storage in rock salts based on new partitions of the surrounding rock. *Environmental Earth Sciences*, 73:6911–6925.
- Małachowska, A., Łukasik, N., Mioduska, J., and Gebicki, J. (2022). Hydrogen storage in geological formations—The potential of salt caverns. *Energies*, 15(14).
- Marketos, G., Spiers, C., and Govers, R. (2016). Impact of rock salt creep law choice on subsidence calculations for hydrocarbon reservoirs overlain by evaporite caprocks. *Journal of Geophysical Research: Solid Earth*, 121(6):4249–4267.
- Masud, A. and Khurram, R. (2004). A multiscale/stabilized finite element method for the advection–diffusion equation. *Computer Methods in Applied Mechanics and Engineering*, 193(21–22):1997–2018.
- Meisel, T., Zill, F., Silbermann, C., Wang, W., Bilke, L., and Kern, D. (2024). Arehs - OpenGeoSys Workflow.
- Nasir, O., Fall, M., Nguyen, T. S., and Evgin, E. (2011). Modelling of the hydro-mechanical response of sedimentary rocks of southern Ontario to past glaciations. *Engineering Geology*, 123(4):271–287.
- Peach, C. J. (1991). *Influence of deformation on the fluid transport properties of salt rocks*. PhD thesis, Faculteit Aardwetenschappen der Rijksuniversiteit te Utrecht.
- Pitz, M., Kaiser, S., Grunwald, N., Kumar, V., Buchwald, J., Wang, W., Naumov, D., Chaudhry, A. A., Maßmann, J., Thiedau, J., Kolditz, O., and Nagel, T. (2023). Non-isothermal consolidation: A systematic evaluation of two implementations based on multiphase and Richards equations. *International Journal of Rock Mechanics and Mining Sciences*, 170(May 2022).
- Rühaak, W., Anbergen, H., Grenier, C., McKenzie, J., Kurylyk, B. L., Molson, J., Roux, N., and Sass, I. (2015). Benchmarking numerical freeze/thaw models. *Energy Procedia*, 76:301–310.
- Rühaak, W., Bense, V. F., and Sass, I. (2014). 3D hydro-mechanically coupled groundwater flow modelling of Pleistocene glaciation effects. *Computers & Geosciences*, 67:89–99.
- Schulze, O., Popp, T., and Kern, H. (2001). Development of damage and permeability in deforming rock salt. *Engineering Geology*, 61(2–3):163–180.
- Spiers, C., Schutjens, P., Brzesowsky, R., Peach, C., Liezenberg, J., and Zwart, H. (1990). Experimental determination of constitutive parameters governing creep of rock salt by pressure solution. *Geological Society, London, Special Publications*, 54(1):215–227.
- Spiers, C. J. and Carter, N. L. (1998). Microphysics of rock salt flow in nature. *Series on Rock and Soil Mechanics*, pages 115–128.
- Stormont, J. and Daemen, J. (1992). Laboratory study of gas permeability changes in rock salt during deformation. In *International journal of rock mechanics and mining sciences & geomechanics abstracts*, volume 29, pages 325–342. Elsevier.
- Toth, J. (1963). A theoretical analysis of groundwater flow in small drainage basins. *Journal of geophysical research*, 68(16):4795–4812.
- Urai, J., Schlöder, Z., Spiers, C., and Kukla, P. (2008). Flow and transport properties of salt rocks. *Dynamics of complex intracontinental basins: The central European basin system*, pages 277–290.
- Urai, J. and Spiers, C. (2017). The effect of grain boundary water on deformation mechanisms and rheology of rock salt during long-term deformation. In *The mechanical behavior of salt—understanding of THMC processes in salt*, pages 149–158. CRC Press.
- Van der Veen, C. J. (2013). *Fundamentals of glacier dynamics*. CRC Press.
- Van Keken, P., Spiers, C., Van den Berg, A., and Muyzert, E. (1993). The effective viscosity of rock salt: implementation of steady-state creep laws in numerical models of salt diapirism. *Tectonophysics*, 225(4):457–476.
- Van Oosterhout, B., Hangx, S., and Spiers, C. (2022). A threshold stress for pressure solution creep in rock salt: Model predictions vs. observations. In *The mechanical behavior of salt X*, pages 57–67. CRC Press.
- Wang, W., Shao, H., Rink, K., Fischer, T., Kolditz, O., and Nagel, T. (2021). Analysis of coupled thermal-hydro-mechanical processes in Callovo-Oxfordian clay rock: From full-scale experiments to the repository scale. *Engineering Geology*, 293.
- Wang, Y. and Zhang, Y. (2023). Effect of Relative Humidity on the Creep Rate of Rock Salt at Intermediate–Low Stresses. *Rock Mechanics and Rock Engineering*, 56(12):8711–8721.
- White, W. A. (1992). Displacement of salt by the Laurentide Ice Sheet. *Quaternary Research*, 38(3):305–315.
- Zill, F., Wang, W., and Nagel, T. (2022). *Influence of THM process coupling and constitutive models on the simulated evolution of deep salt formations during glaciation*. CRC Press. Pages: 353–362 Publication Title: The Mechanical Behavior of Salt X.

*Manuscript received 7th June 2024, revised 26th September 2024 and 29th October 2024, accepted 29th October 2024.*